UCLA
UCLA Previously Published Works

Title

Platinum Surface Water Orientation Dictates Hydrogen Evolution Reaction Kinetics in Alkaline Media.

Permalink

Authors

Shah, Aamir Hassan
Zhang, Zisheng
Wan, Chengzhang
et al.

Publication Date

DOI

Copyright Information

Peer reviewed

The platinum-surface water orientation dictates hydrogen evolution reaction kinetics in alkaline media

Aamir Hassan Shah[1]†, Zisheng Zhang[1]†, Chengzhang Wan[1,2], Sibo Wang[1], Laiyuan Wang[1], Anastassia N. Alexandrova[1,3,*], Yu Huang[2,3,*], Xiangfeng Duan[1,3,*]

[1]Department of Chemistry and Biochemistry, University of California, Los Angeles; California 90095, United States.

[2]Department of Materials Science and Engineering, University of California, Los Angeles; California 90095, United States.

[3]California NanoSystems Institute, University of California, Los Angeles; California 90095, United States.

†*These two authors made equal contributions*

*Correspondence: xduan@chem.ucla.edu, yhuang@seas.ucla.edu, ana@chem.ucla.edu

The hydrogen evolution reaction (HER) on platinum (Pt) surface typically displays a distinct dependence on electrolyte pH and is notably more sluggish in alkaline electrolyte compared to acid. The fundamental molecular level understanding of HER kinetics in alkaline media remains a topic of considerable debate. Herein, we combine cyclic voltammetry (CV) and electrical transport spectroscopy (ETS) approach to probe Pt surface at different pH and develop molecular level insights on the HER kinetics in alkaline media. The pH-dependent studies reveal a sharp switch of the HER Tafel slope from ~110 mV/decade in pH 7–10 to ~53 mV/decade in pH 11–13, suggesting considerably enhanced Volmer kinetics at higher pH. The ETS studies reveal a similar pH-dependent switch in the ETS conductance signal at around pH 10, suggesting a notable change of surface adsorbates. Fixed-potential density functional calculations and chemical bonding analysis suggest that such a switch can be attributed to a change of interfacial water molecule orientation from the O-down to H-down configuration when the pH is increased above 10, which weakens the O–H bond in the interfacial water molecules and boost alkaline HER kinetics. Our integrated experimental and theoretical studies for the first time reveal direct evidence supporting the reorganization of interfacial water molecule configuration at pH~10 and provide an unprecedented molecular level understanding of the non-trivial pH dependent HER kinetics in alkaline media.

Hydrogen evolution reaction (HER) is a key process for water electrolysis and green hydrogen production from renewable energy sources[1,2]. The HER kinetics on platinum (Pt) surface typically displays a distinct dependence on electrolyte pH. In particular, it is well recognized that HER kinetics on Pt surface in alkaline media is substantially slower than in acidic media[3-5], which has been attributed to a change of proton donor from H_3O^+ in acidic conditions to H_2O in alkaline conditions[6-8]. Our recent studies in acidic and neutral electrolytes revealed that the switch of proton source occurred at a pH around 4 instead of acid/base boundary, which is the attributed to a change of Pt surface-H_2O protonation status and associated with Pt surface hydronium pKa (4.3) (ref.[7]). However, the change of proton source from H_3O^+ to H_2O cannot explain HER activity difference in alkaline media.

In parallel, the hydrogen binding energy (HBE), widely accepted as a thermodynamic descriptor of the HER activity, has been frequently used to interpret the pH-dependent HER kinetics[1,9-14]. For example, Sheng $et\ al.$[1] and Durst $et\ al.$[15] independently suggested that HBE derived from the pH-dependent hydrogen underpotential deposition (H_{upd}) peak may serve as an effective descriptor for interpreting pH dependent HER kinetics. However, it has been argued by Koper and coworkers that the H_{upd} peak is not solely associated with the hydrogen adsorption but also convoluted with the hydroxide desorption on step sites[16]. Thus, the pH dependent H_{upd} peak potential is not an unambiguous indicator of the HBE.

To this end, Koper $et\ al.$ introduced potential of zero free charge (pzfc) theory to explain the different HER kinetics in acid and alkaline media[3]. They argued that in acidic media, the pzfc is closer to the HER region and reorganization energy of interfacial water associated with transporting a proton through electrical double layer is smaller and hence the HER kinetics is more facile[3]. Whereas, in alkaline media the pzfc is far from the HER region (i.e., closer the OH_{ad} region), leading to a stronger electric field in HER region and a larger interfacial water reorganization energy, which impedes OH^- transfers through double layer[3]. However, the pzfc theory cannot explain the higher HER kinetics at pH 13 compared to pH 7 as the reorganization energy at pH 13 is expected to be considerably larger than that at pH 7 (ref.[17]). Besides the aforementioned theories, it has also been suggested that the other factors including water dynamics[18,19], transport of related intermediates (H_2O^*/OH^*) at the electrode/electrolyte

interface[20,21] and interfacial hydrogen bond networks[22] in alkaline media may also play a critical role in HER kinetics.

Despite extensive aforementioned efforts in comparing the acidic and alkaline media, the HER kinetics within the alkaline (pH > 7) media was often considered pH independent on Pt (111) surface[6,23] and much less explored[17,24-26]. Koper *et al.* recently investigated the pH-dependent HER kinetics on an Au electrode in the alkaline media, found higher HER activity at higher pH, and attributed it to the increased local cations concentration at higher pH that stabilizes the transition state of the rate-determining Volmer step via a favorable interaction with the dissociating water molecule (*H–OH$^{\delta-}$–cation^{+})[17]. Likewise, Qiao *et al.* attributed the higher activity in high-pH electrolytes to the locally generated H_3O^+ intermediates that create a unique acid-like local reaction environment on nanostructured catalytic surfaces and reduce the energy barrier for the overall reaction[24]. Recently, Surendranath *et al.* also observed a decrease of HER overpotential on Au and Pt electrodes with increasing pH above 10, although the underlying reason was not substantially discussed[25]. Despite these interesting studies and suggestions, a molecular level understanding of the HER on Pt electrode in alkaline media has not been developed due to the lack of robust experimental techniques that can reveal molecular level insights across the Pt-electrolyte interface.

Herein, we address this issue by systematically studying the HER kinetics in non-buffered alkaline media (pH 7 – 13) on polycrystalline Pt electrode surface. Our systematic studies reveal a sharp switch of Tafel slope (from ~110 mV/decade below pH 10 to ~53 mV/decade above pH 10) and exchange current density (from ~ 0.002 mA/cm^2 below pH 10 to > 0.5 mA/cm^2 above pH 10), signifying a switch of the HER kinetics. We further employed electrical transport spectroscopy (ETS) to reveal the molecular level insights on interfacial water structure on Pt surface. The ETS conductance signal reveals nearly constant conductance below pH 10, and a notable increase above pH 10, suggesting a change in surface speciation in these two distinct pH regimes. Static and dynamic fixed-potential (FP) density functional theory (DFT) calculations show that the interfacial water molecules adopt the O-down configuration below pH=11 and flip to the H-down configuration above pH=11, correlating well with the experimentally observed switch of HER kinetics and ETS signals. **The switching of the interfacial water molecule orientation to H-down configuration changes the partial charge distribution and weakens the O–H bond in the interfacial water molecule, which accelerates alkaline Volmer kinetics**. This excellent correlation of the experimentally observed switch in Tafel slope, exchange current

3

density and the ETS conductance signal, with the theory-predicted water orientation change, for the first time, provides a robust molecular-level interpretation of the pH-dependent HER kinetics on Pt surface in alkaline media. Such molecular level understanding will be instrumental in guiding further fundamental understanding and eventually the rational design of optimized electrode-electrolyte conditions for alkaline electrolysis.

Results

pH dependent voltammetric characteristics and HER activity

The pH dependence of the HER kinetics is an intriguing topic. If we assume protons (hydroniums) as the reactant ($H_3O^+ + e^- + * \rightarrow H_{ad} + H_2O$), the thermodynamic onset potential for HER is expected to be constant on the RHE scale but negatively shifts 59 mV for each pH increase in the normal hydrogen electrode (NHE) scale ($E_{RHE}=E_{NHE} + 0.059$ pH), according the Nernst equation ($E = E^0 - 0.059$ pH). On the other hand, the situation could be different in the neutral or alkaline condition, in which the Volmer step ($H_2O + e^- + * \rightarrow H_{ad} + OH^-$) is believed to be the rate limiting. In this case, the onset potential is expected to be independent of the electrolyte pH (thus constant on the **NHE** scale) because no proton or hydroxide is involved on the reactant side. It has been previously suggested that HER in alkaline media does not involve protons, and one should not expect a pH dependence[6,23]. Thus, a plot on the NHE scale has been frequently used for alkaline media[6,23]. We investigated the voltammetric response of HER on a Pt surface using cyclic voltammetry (CV) in alkaline media of different pH between 7-13. Our CV studies reveal that the H_{upd} peak potential from pH 7 to pH 9 is largely independent of pH value, showing a nearly constant peak position or onset potential in the NHE scale (Fig. 1a), while the H_{upd} peaks in pH 11-13 show clear pH dependence and thus were compared on the pH dependent RHE scale (Fig. 1b). The CV of pH 10 is showing a transition from pH independent to pH dependent H_{upd} peaks and hence presented both on the NHE and RHE scale as a reference point. Overall, the H_{upd} peak intensity increases with increasing pH and is significantly larger above pH 10. Likewise, the HER polarization curves in pH 7-9 is largely pH independent (Fig. 1c) and show similar HER onset potential on the NHE scale, whereas show a clear pH dependence in pH 11-13 with a comparable onset potential on the RHE scale but an apparently increase HER activity with increasing pH (Fig.1d). Previous studies of nanostructured Pt[24] or Au[17] electrodes have also shown a similar increase of HER activity with increasing pH in alkaline media[25,26]. We note that there is a study

reporting a decrease of HER activity on Pt(111) electrode with increasing pH from 11 to 13 (Ref.[3]), which is intriguing but not confirmed by other studies yet, to the best of our knowledge.
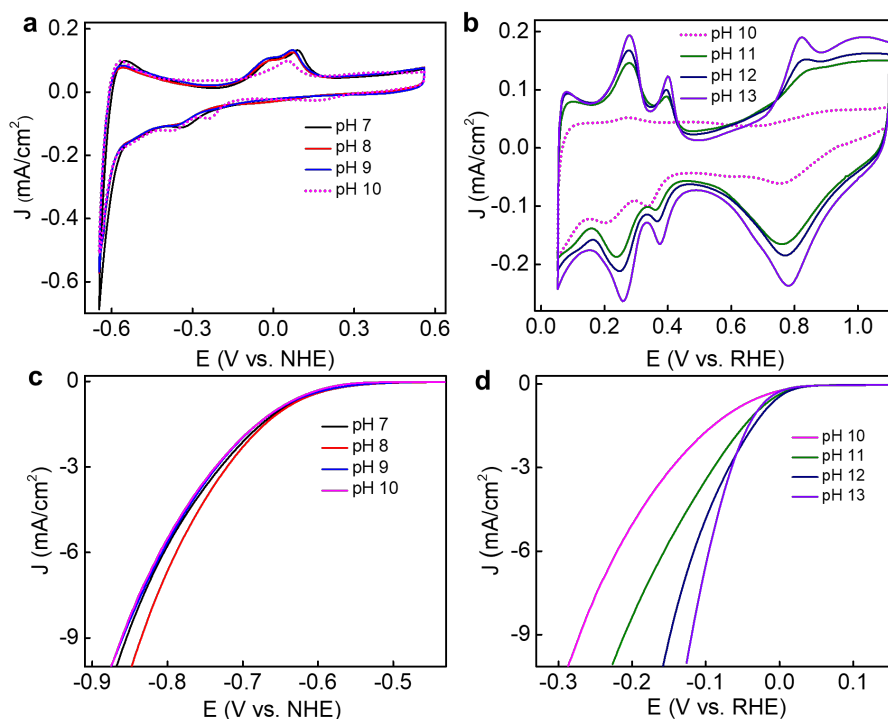
Fig. 1| Voltammetric studies in 0.1 M electrolyte solution with different pH. (a) CV on stationary Pt disc electrode in N_2-saturated electrolyte of pH 7, 8, 9 and 10 versus pH independent NHE scale and **(b)** pH 10, 11, 12 and 13 versus pH dependent RHE scale at scan rate of 100 mV/sec (pH was adjusted by KOH and $HClO_4$) **(c)** IR-corrected HER polarization curves collected in N_2-saturated electrolyte solution of pH 7, 8 and 9 versus pH independent NHE scale and **(d)** pH 10,11,12 and 13 versus pH dependent RHE scale at scan rate of 5 mV/sec with rotation rate of 1600 rpm (electrolyte concentration was maintained 0.1 M in all cases and the pH was adjusted by 0.1 M KOH and 0.1 M $HClO_4$).

Considering the potential ambiguity of the NHE to RHE conversion, the Tafel slope and exchange current density give a more reliable evaluation of the reaction kinetics (Fig. 2 a,b). Importantly, **the Tafel slopes and exchange current densities show an apparent transition at pH 10 (Fig. 2b). In particular, the Tafel slopes display a notable switch from a value of ~110 mV/decade below the pH 10 to ~53 mV/decade above pH 10 (Fig. 2b), suggesting a switch of rate determining step at around pH 10 and a more favorable HER kinetics at higher pH alkaline media.** Likewise, the exchange current density versus pH plot also showed two distinct regimes: a much lower value of ~ 0.002 mA/cm^2 in the electrolyte of pH 7 to 9 indicating slower kinetics in the neutral pH regime. At pH 10, the intrinsic HER/HOR activity starts to increase with the exchange current density value of ~0.1 mA/cm^2, which reaches beyond ~ 0.5 mA/cm^2 at pH

5

11-13. This trend is largely similar to the Tafel slope. The slightly lower exchange current density and larger Tafel slope in case of pH 13 compared to pH 11 and 12 is attributed to the higher local cation concentration at the interface (due to higher pzfc and larger interfacial electrical field)[3] that negatively impacts the HER/HOR kinetics.
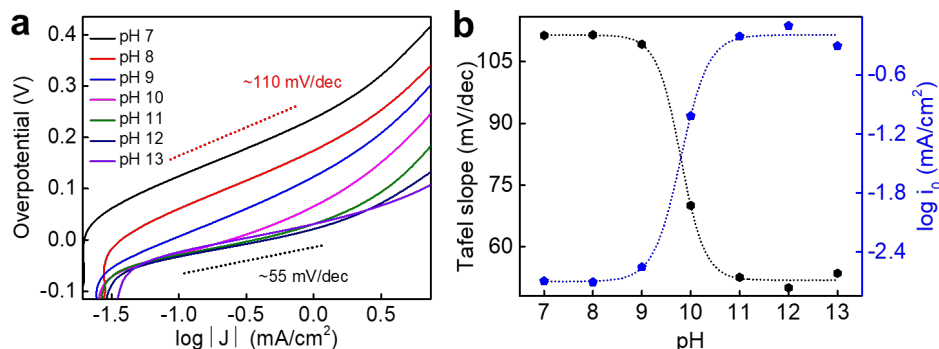

Fig. 2| Tafel slope and exchange current density in 0.1 M electrolyte solution at different pH. (a) Tafel plots in different pH electrolyte collected on Pt disc electrode with rotation rate of 1600 rpm at a scan rate of 5 mV/sec in N_2-saturated 0.1 M ionic strength electrolyte solution (pH was adjusted by KOH and $HClO_4$) and **(b)** Plot of Tafel slope values and exchange current density versus electrolyte pH (the dotted lines are guide to eyes).

On chip in-situ monitoring of the pH dependent Pt-surface adsorbates

To understand the molecular level origin of the non-trivial pH dependence of HER kinetics in alkaline media, we employed electrical transport spectroscopic (ETS) studies to directly probe the Pt surface adsorbates at different pH. Using ultrafine Pt nanowires (PtNWs) as a model catalyst [7,27,28], the ETS approach involves a concurrent measurement of the PtNWs conductance during electrochemical studies at different electrochemical potentials (Supplementary Fig. 1 and ref.[27] for detailed working principle of the technique). In general, the conductance of the ultrafine metallic PtNWs measured in ETS studies is highly sensitive to the exact surface adsorbates due to surface scattering of the conduction electrons, but insensitive to the electrostatic or electrochemical potential. The ETS approach thus offers a unique signal transduction pathway to exclusively probe the surface adsorbates, with minimum interferences from the electrochemical potentials or the bulk electrolyte environment, which is difficult to achieve with other analytic approaches that are often convoluted with or dictated by the near surface (e.g., electrical double layer) and bulk electrolyte background.

The ETS studies show the PtNWs generally exhibit a lower conductance in the hydroxide adsorption/desorption potential regime, which is attributed to the more pronounced scattering of

the conduction electrons by the strongly bonded OH_{ad}/O_{ad} on the Pt surface in this potential regime[29]. Sweeping the electrochemical potential to the negative direction results in a gradual change of surface adsorbates and thus the corresponding conductance behavior: (i) in the EDL region, the OH_{ad}/O_{ad} are replaced by interfacial H_2O molecules, which reduces the electron scattering and results in an increase in conductance; and (ii) further sweeping of the electrode potential to negative direction, the interfacial H_2O is largely replaced by H_{ad} that further reduces the scattering and increases the conductance.
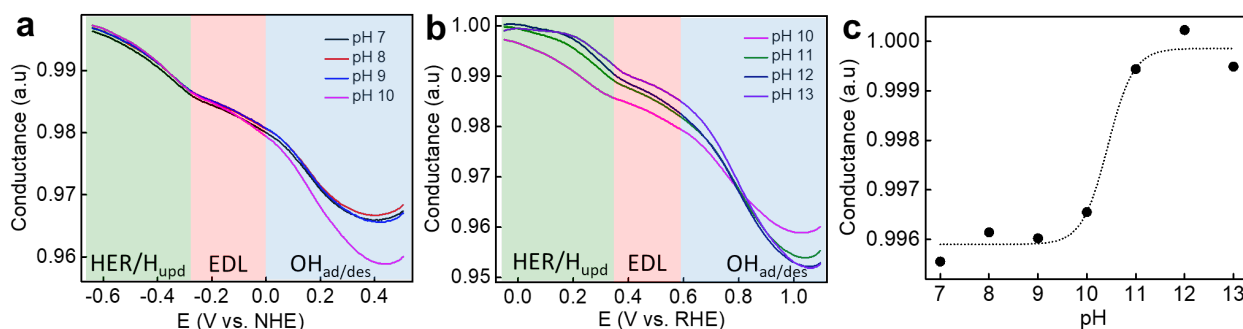
Fig. 3| Electrical transport spectroscopy (ETS) measurements (a) ETS spectra in pH 7-10 versus NHE scale, **(b)** pH 10-13 versus RHE scale in 0.1 M electrolyte (ionic strength and pH was maintained by KOH and $KClO_4$) and **(c)** Plot of conductance versus electrolyte pH at -0.59 V versus NHE (from pH 7-10) and 0 V versus RHE (from pH 10-13) (the dotted line is guide to eye).

The ETS studies in electrolytes with different pH reveal that the conductance is nearly constant in the electrical double layer regime (EDL) and HER/H_{upd} potential regime in the electrolyte of pH 7-9 indicating little change in surface speciation on Pt surface within this pH range (Fig. 3a). The shape of the ETS signal at and above pH 10 display notably different characteristics (Fig. 3b). In particular, the conductance showed an increase above pH 10 in the EDL and HER/H_{upd} potential regime (Fig. 3b). A plot of the conductance in the HER regime versus pH shows a nearly constant conductance from pH 7-9 and a steep rise of the conductance with increasing pH above 10 (Fig. 3c). Considering the surface adsorbates in the EDL region is dominated by H_2O_{ad} [30], **such an increase of the conductance suggests a change in H_2O_{ad} configuration, likely from a more scattering (lower conductance) O-down configuration at lower pH to a less scattering (higher conductance) H-down configuration at higher pH.** The flipping behavior is also in line with previous experimental reports[33]. Interestingly, this switch in the ETS conductance signal at around pH 10 is largely consistent with the evolution of the pH-dependent HER Tafel slopes. The transition point in ETS results indicate that there is an abrupt

change in surface speciation at pH 10, which leads to a switch in HER kinetics (Tafel slope) from a Volmer-step dictated kinetics (with the Tafel slope of ~110 mV/dec) below pH 10 to a Heyrovsky-step-dictated kinetics (Tafel slope ~ 53 mV/dec) above pH 10.

Theoretical insight into the role of pH on surface adsorbates

We performed theoretical calculations to further understand the change in surface speciation and explore the molecular level origin of the switch in HER kinetics. To probe the nature of the interfacial structural transition that underlies the switching behavior, we used the fixed-potential density functional theory (FP-DFT) technique to locate the most stable adsorption configuration of water on Pt(111) at 0 V_{RHE} in the pH range of 7 to 14 (Supplementary Fig. 2) [31]. Our calculations show that the adsorbed water adopts an O-down configuration below pH=11 but switches to the H-down configuration above pH=11 (Fig. 4a). As a result of the configurational change, the Pt…O distance increases from ca. 2.4 Å to 3.3 Å, and the angle between the H_2O orientation (defined by the vector from O to the midpoint of H's) and the Pt surface normal increases from ca. 60° to 170° (Fig. 4b).

To better describe the realistic solvation and dynamics at room temperature[32], we further performed ab initio molecular dynamics (AIMD) with an explicit water slab of ca. 10 Å thickness and fixed-potential (FP) treatment (Supplementary Fig. 3 and 4), and compared the spatial distribution of O and H atoms (relative to the Pt surface) at selected pH (Fig. 4c). As pH increase from 7 to 10, the first O peak at ca. 2.2 Å stays sharp and high, suggesting a large population of directly O-adsorbed water. The H peak at 2.6 Å is significantly higher than the one at 2.1 Å, suggesting the O-down orientation in the contact layer to be dominant. As the pH increases from 10 to 11, the intensity of the first O peak is significantly reduced, suggesting a weakening of the water adsorption via Pt—O. Moreover, the intensity of the H peak at ca. 2.1 Å (corresponding to H-down water) builds up to a comparable level to that of the O-down at pH 11 and becomes dominant beyond pH=12, **suggesting a flip of the majority of water molecules in the contact layer**. Such a flip is better visualized by the distribution map of water orientation angles (Fig. 4d): the adsorbed O-down water (marked by region A) is depleted as the pH increases, and the majority of the interfacial waters shifts from a O-down orientation (Region B) to a H-down orientation (Region C) . The flipping from O-down confuguration to H-down configuration upon increasing pH is consistent with a swtich from low conductance state at lower pH to a higher conductance

state at higher pH observed in the ETS studies, in which the O-down configuration shows stronger electron scattering and thus lower conductance than the H-down configuration.
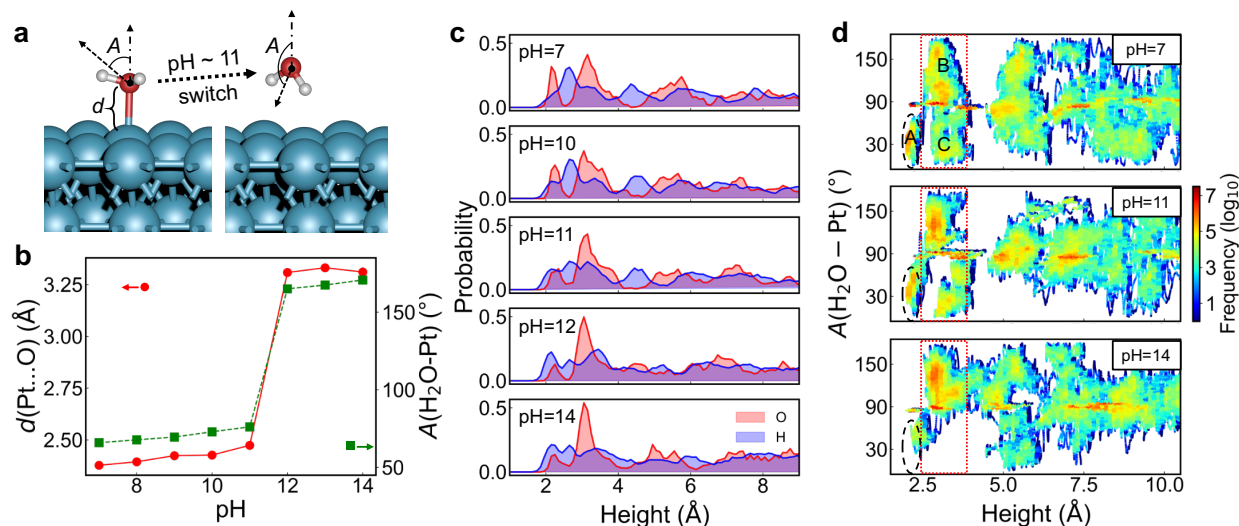

Fig. 4| Static and dynamic fixed-potential DFT calculations of interfacial structure of Pt(111)/water. (a) Structural models of low-pH and high-pH water configurations on Pt(111), with key geometric parameters marked. **(b)** The Pt-O distance and the water orientation angle in pH range of 7 to 14. **(c)** Spatial probability distribution of O and H in water with respect to relative height to Pt surface from fixed-potential ab initio MD simulations at selected pH levels. **(d)** Statistics of water orientation angle with respect to relative height to Pt surface at selected pH levels. The regions corresponding to adsorbed water (region A) and the contact water layer (region B and C for H-down and O-down waters) are marked by black dashed circle and red dotted box, respectively.

The sharp crossover behavior at ~ pH 11 (Fig. 4) closely resembles the experimental pH dependence of HER Tafel slope, exchange density (Fig. 2b), which inspires us to quantify the influence of water configurational change on the HER activity. To this end, we performed Crystal Orbital Hamilton Population (COHP) analysis on selected atomic pairs in the pH range of 7 to 14. The obtained COHP is integrated up to Fermi level to yield negative integrated COHP ($-\mathrm{ICOHP}_{E_F}$), which acts at a descriptor of the strength of covalent or noncovalent interactions (Fig. 5a). It was observed that the Pt…O gradually weakens as the pH increases from 7 to 11, and sharply reduces to 0.02 eV at pH=11 and stays nearly constant thereafter. The Pt…H, however, is strengthened from 0 to 0.08 eV after the orientational change from O-down to H-down, suggesting a stronger interaction between H in water and the Pt surface at higher pH.

Moreover, the O-H bond in interfacial water is significantly weakened by ca. 0.50 eV in terms of $-\mathrm{ICOHP}_{E_F}$ upon the orientational change (Fig. 5b). The change in effective pK_a of H-down water is estimated, by the fitted correlation between experimental pK_a and calculated

9

−ICOHP$_{E_F}$ (Supplementary Fig. 5), to be 8 units lower than the neutral O-down case, which agrees reasonably well with acidic-like kinetics suggested in previous experimental reports[34,35]. In addition, the H-down water could act as a relay for protons in the outer water layers to cascade to the Pt surface via a hydronium-like intermediate, which is also in line with recent reports of higher local concentration of hydronium species near the Pt surface in high pH conditions [24]. Therefore, more facile Volmer kinetics is expected beyond pH=11 due to the orientational change, which, results in the switch of Tafel slope to a smaller value (Fig. 2b).
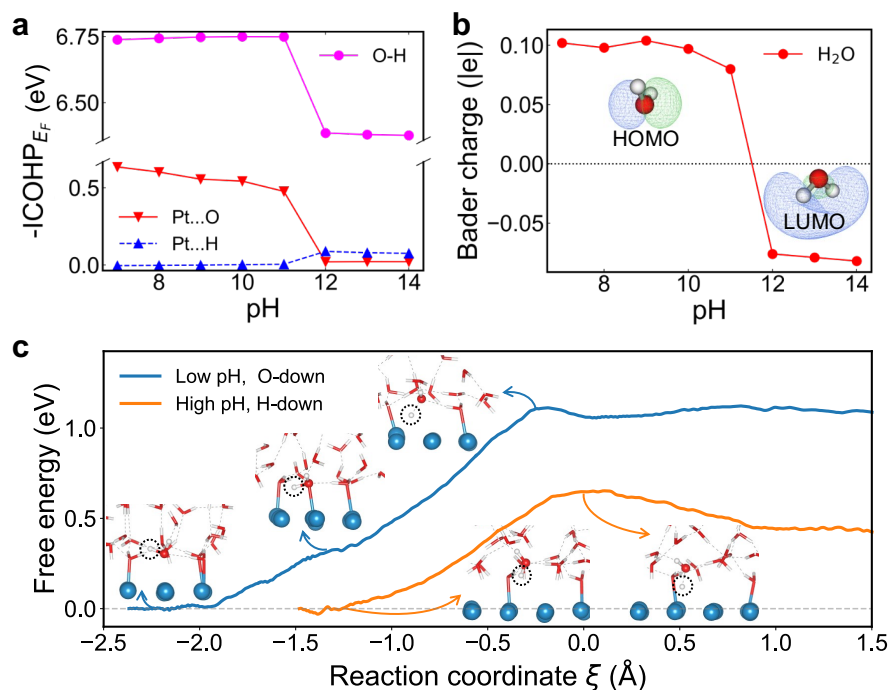
Fig. 5| Influence of interfacial water orientation on water dissociation reactivity. (a) The bond strength descriptor, -ICOHP (negative integrated Crystal Orbital Hamilton Population) up to Fermi level, for Pt…O, Pt…H, and O-H in pH range of 7 to 14. **(b)** Net Bader charge on H$_2$O at the Pt surface in the pH range of 7 to 14, with HOMO and LUMO of water shown as insets. **(c)** The free energy profile of water dissociation for H-down water at low pH and O-down water at high pH. The transferred H is marked by dotted black circles. Notable configurations along the reaction coordinate are shown as insets.

The molecular origin of the O-H weakening is further analyzed by Bader charge analysis (Fig. 5b) and molecular fragment analysis (Supplementary Fig. 6). The net charge of water is ca. +0.10 |e| in the O-down and −0.06 |e| in the H-down configurations. The partial charging of interfacial water at higher pH can be attributed to the charge redistribution caused by shift of the work function of the surface. **Due to the non-bonding nature of the HOMO (O 2p lone pair), partial removal of electron from it has little influence on the O-H bond strength. On the other**

hand, the LUMO in water has O-H σ* characteristics (Fig. 5b inset), and the filling of this orbital would directly lead to a weakening of O-H bond, as is evidenced by a decrease in Mayer bond order from 0.9 to 0.24 per electron. The diffuse nature of the H-side lobe of the HOMO also promotes the interaction between H in water and the Pt surface.

To quantify the influence of interfacial water configuration on the kinetics of water dissociation, we performed free energy calculations by slow-growth constrained MD sampling and thermodynamic integration within the FP-AIMD scheme (see Computational Details and Supplementary Note 1 for details). Our calculations show that the O-down water at low pH needs to rotate to a flat configuration before it can break the O-H bond and transfer the H to the Pt surface, with a rather high free energy barrier of 1.10 eV (Fig. 5c). In contrast, the H-down water at high pH do not need to go through this extra step and can directly dissociate with a much lower free energy barrier of 0.55 eV. In other words, the interfacial polarization and reorientation of interfacial water molecules to the H-down configuration at high pH not only electronically weakens the O-H in water, but also modifies the water dissociation reaction pathway by skipping an intermediate flat configuration, thus greatly reducing the kinetic barrier and leading to considerably improved HER activity.

Additionally, we note that near-surface hydroxide may also play a role in modifying the reaction kinetics, although for technical reasons it is infeasible to explicitly include solvated hydroxide in the FP-AIMD. To explore this effect, we can derive the difference in thermodynamics of hydroxide binding on the surface from the trajectory averages with and without *OH, assuming the initial state of hydroxide (solvated in the bulk electrolyte) to be pH-independent, so that we can cancel out the energy of the solvated state. In this case, our calculations reveal that the hydroxide binding with Pt at higher pH (where the majority of interfacial waters are H-down) is stronger than that at lower pH (where the majority of interfacial water are O-down) by 0.25 eV. This indicates the role of interfacial water orientation in stabilizing more surface hydroxide (via water deprotonation or other means) at higher pH values. Such surface hydroxide could also function as electronically favored proton acceptors and geometrically favored proton donors for interfacial H-down water to promote water dissociation [29].

Conclusions

In summary, we have performed surface-sensitive electrical transport spectroscopy measurements as well as static and dynamic fixed-potential DFT calculations to understand the molecular level origin of the pH-dependent HER activity on Pt surface in alkaline media. The intriguing switching behavior in the pH dependence of interfacial conductance and Tafel slope at ca. pH=10 suggest a reorganization of interfacial water molecule structure and a change in HER mechanism. Static and dynamic calculations reveal a sharp orientation transition of interfacial water from the O-down to H-down configuration, which, as further shown by chemical bonding analysis, leads to weakened O-H bond and enhanced HER kinetics. Our theoretical results show that the hydroxide binding with Pt at high pH (where the majority of interfacial water are H-down) is stronger than the case at low pH (where the majority of interfacial water are O-down) by 0.25 eV. Such surface hydroxide could also function as electronically favored proton acceptors and geometrically favored proton donors for interfacial H-down water to promote water dissociation. The excellent correlation among experiment and theory provides, for the first time, a robust interpretation of the pH-dependent HER kinetics on Pt surface in alkaline media. These studies provide a pathway toward a more complete understanding of pH effects on the electrode/water interfacial structure and their critical role in the relevant electrochemical reactions and renewable energy conversion.

Methods

1. Experimental Methods

Chemicals

Potassium hydroxide (KOH, 87.4%), potassium perchlorate (KClO$_4$, 99%) and perchloric acid (HClO$_4$, 70%, PPT grade) were all purchased from Thermo Fisher Scientific. All aqueous solutions were prepared using deionized (DI) water (18.2 MΩ·cm) obtained from an ultrapure purification system (Aqua Solutions).

Electrochemical Measurements

All of the electrochemical measurements were performed using typical three electrode setup. Platinum rotating disk was used as working electrode, Pt wire and Ag/AgCl were used as the counter and reference electrodes, respectively.

Synthesis of Pt nanowires (PtNWs)

PtNWs were synthesized as reported previously[27]. Briefly, a mixture of KOH (0.6 g) and ethylene glycol (4 ml) was dissolved in DMF (6 ml). Aqueous solution of K_2PtCl_6 (8 wt%, 0.1 ml) was then added into the mixture. After stirring for 20 min, the reaction mixture was transferred into a Teflon-lined autoclave, which was maintained at 150 °C for 15 h and then cooled to room temperature. The black powders were collected after the reaction and washed with ethanol and deionized (DI) water repeatedly for several times before use.

Preparation of PtNWs films

A free standing PtNWs film was assembled on chip from as-prepared PtNWs suspension by a co-solvent evaporation method [27]. Briefly, PtNWs suspensions in ethanol (400 μl, 0.4 mg ml^{-1}) was added dropwise into a beaker (about 9 cm in diameter) filled with DI water. A thin film of PtNWs from top of water surface was then transferred onto the device.

Fabrication of the PtNWs electrochemical device

The device fabrication was followed by the similar approach as previously reported by our group [27]. Typically, a PMMA (A8, MicroChem Corp.) film was prepared by spin coating on the substrate (p++ silicon wafer with 300 nm thermal oxide) surface with pre-patterned Au electrodes (Ti/Au, 10/50 nm). E-beam lithography was then used to open windows on PMMA, which created desired patterns on the substrate. After the removal of PMMA template, PtNWs was deposited on the device substrate with desired patterns. To rule out the influence of electrolyte and to avoid electrochemical reactions on the Au electrodes, another layer of PMMA (~500-nm thick, electrochemically inert) was then deposited on the PtNW device with spin coating. A smaller window that only exposes PtNWs was opened by e-beam lithography. The device was finally used for in-device electrochemistry and *in situ* electrical transport spectroscopy measurement.

In-device CV and *in situ* ETS

A two channel SMU (Agilent B2902a) was used for the measurement. The first SMU channel was used as a potentiostat to control the potential of source electrode as to the reference electrode (V_G), while collecting the current (I_G) through the counter electrode with a scan rate of 50 mV/sec. The second channel was used to supply a small voltage of (10 mV) between source and drain electrodes and collecting the corresponding current (I_{SD}).

The electrical conductivity of the metallic PtNWs is sensitive to surface environment, due to surface scattering of the conduction electrons, producing a resistance change following equations [27]:

$$\rho = \rho_0 \left(\left(\frac{1-p}{1+p} \right) \times \frac{\lambda}{d} \right) \quad (d \ll \lambda) \tag{1}$$

Here ρ and ρ_0 are the resistivity of the one dimensional PtNWs and bulk metal respectively, λ is the mean free path of electron, d is the nanowire diameter, and p is a specularity parameter with a value ranging from 0 (for highly diffusive scattering) to 1 (completely specular scattering) (Supplementary Fig. 1b)[36]. When the diameter (d) of the PtNWs is smaller than the electron mean free path ($\lambda \sim 5$ nm)[36], their resistance is highly dependent on the exact surface adsorbate that modifies the value of specularity (p). It is important to note such surface scattering is exclusively sensitive to surface adsorbates, with little impact for the electrostatic or electrochemical potential. For example, previous studies have clearly shown a constant conductance at different electrochemical potentials when there is a stable surface adsorbate layer (*e.g.*, CO or I$^-$) that does not change with potential[27,28], clearly demonstrating the insensitivity of the metallic PtNWs to the varying electrochemical potentials. Thus, the ETS approach offers a unique signal transduction pathway to exclusively probe the surface adsorbates, with minimum interferences from the electrochemical potentials or the bulk electrolyte environment, which is difficult to achieve with other analytic approaches that are often convoluted with near surface (e.g., EDL) or bulk electrolyte background.

We have first closely compared the ETS measurement with the corresponding CV curve at pH 13 when the potential is gradually changed from 1.10 – 0.05 V *vs.* RHE (Supplementary Fig. 1c), which consistently shows three distinct regions: (i) O/OH$_{ad/des}$ region (1.10-0.60 V vs. RHE); (ii) electrical double layer region (OH$_{ad}$ replaced by H$_2$O) (0.60-0.40 V vs. RHE); and (iii) H$_{upd}$ and HER regime (0.40-0.05 V vs. RHE). The lowest conductance observed in the high potential regime is attributed to the larger scattering from the strongly bonded OH$_{ad}$ on the Pt surface, which significantly reduces the conductance of the PtNWs. Scanning the potential toward lower potential regime results in a monotonic increase in conductance due to the gradual replacement of the OH$_{ad}$ by H$_2$O. The conductance increase slowed in the double layer regime where Pt surface are nearly completely reduced and most of the OH$_{ad}$ are replaced by H$_2$O. Further sweeping the potential to

the more negative regime results in H_{upd} on electrode surface (replacement of surface adsorbed H_2O and residue OH_{ad} by H_{upd}), which further reduces scattering and increases conductance. The conductance eventually saturates at a nearly stable value below 0.15 V *vs.* RHE (beyond the H_{upd} peak in CV) due to the formation of a complete hydrogen monolayer adsorption.

2. Computational Details

Model Set-up

In the static calculations, the Pt/water electrochemical interface is modelled by an orthogonalized 4-layer 4x4 supercell of Pt(111) termination with one water molecule adsorbed atop. The bottom two layers of the Pt slab are constrained as bulk region, and everything else is allowed to relax as the interface region. A vacuum slab of the 15 Å thickness is added in Z direction to avoid spurious interactions between periodic images.

In the molecular dynamics simulations, 36 explicit water molecules (water slab is c.a. 10 Å thick) are placed above the Pt(111) surface for more realistic description of the interfacial solvation structures. The water configurations are pre-equilibrated using TIP4P force field [37]. Hydroxide is introduced by removing one H from a surface-adsorbed water.

Electronic Structure Methods

The periodic electronic structure calculations are performed with density functional theory, using PBE functional[38] and PAW pseudopotentials[39] implemented in the VASP program (version 5.4.1) [40-43]. D3 correction is used to better account for the dispersion interactions [44]. The convergence criterion for SCF electronic minimization is set to 10^{-5} eV. Due to the relatively large system and sampling size, only the Γ *k*-point is sampled in the reciprocal space of the Brillouin zone throughout, and the cutoff energy for the kinetic energy of the plane-waves was 400 eV.

The solvation effect and electrolyte distribution beyond the slab regions are described implicitly by a polarizable continuum with linearized Poisson-Boltzmann model as implemented in VASPsol code [45]. The dielectric constant is taken as 78.4 (water), and the Debye length is taken as 3 Å.

All periodic electronic structure analyses are performed based on converged charge density or wavefunction. The Bader charges are calculated using Bader Charge Analysis program [46]. The COHP analysis is performed using LOBSTER program with the pbeVaspFit2015 basis set [47].

The molecular fragment calculations are performed with ωB97X-D functional[48] and def2-TZVP basis sets[49] using the Gaussian 16 program[50] (Revision C.01). Molecular orbital visualization and Mayer bond order analysis are performed using the Multiwfn program[51] on the converged wavefunctions from DFT calculation.

Fixed-potential Treatments

Under a constant electrode potential, the electrode surface is effectively a grand canonical ensemble of electrons where the system can exchange electrons with the electrode (electron reservoir) until the work function of the system aligns with the electrode potential. This treatment has been demonstrated to be necessary in investigating the potential-dependent geometric changes and energetics at an electrochemical interface [31,52].

Here we use the fixed-potential method as implemented in the EChO Python package (https://github.com/zishengz/echo). To be specific, the number of electrons is being optimized in an outer iteration after SCF convergence of each ionic step (geometry optimization step or MD step) to adjust the work function of the system to align with the given electrode potential. This treatment does not depend on the constant capacity approximation or interpolation and hence can exactly capture the potential-dependent geometric changes and the resulted shift in potential of zero charge and effective capacity.

Due to difficulty in continuously adjusting the number of hydroxide ions in the explicit solvation model within the pH range of interest, the pH effect at a constant potential in RHE scale is modeled by shifting the potential in SHE according to the Nernst equation:

$$U_{\text{RHE}} = U_{\text{SHE}} + \ln 10 \; k_{\text{B}} T \; \text{pH} \tag{2}$$

Fixed-potential *ab initio* Molecular Dynamics Simulations

The ab initio molecular dynamics simulations are performed on the pre-equilibrated structures and with the same DFT settings as in the geometry optimization. The nuclear motions are treated under the Born-Oppenheimer approximation. The simulation is performed within the NVT ensemble at 300 K using the Langevin thermostat (with a friction coefficient of 0.1) which has been demonstrated to cause the least inconsistency of local temperature in solid/liquid interfacial models [53]. To study the interfacial dynamics at different pH at the save potential in RHE scale

(corresponding to different potential in SHE scale), the fix-potential treatment is introduced by performing a potentiostating step (adjusting the number of electrons in the system by time a factor of 0.5 e/V to the difference from the target potential) after each nuclear motion.[54] The analysis of pair radial distribution function and coordination numbers are performed using the VMD software [55].

The free energy profile of water dissociation under the fixed-potential condition are obtained by sampling along the reaction coordinate ξ for an interfacial water molecule. The configurational samplings are performed using the slow-growth technique where ξ is varied sufficiently slow (0.001 Å *per* MD step) to equilibrate all degrees of freedom other than the reaction coordinate, which in the end yields a well-sampled blue moon ensemble. Thermodynamic integration is performed within the blue moon ensemble to obtain the free energy gradient along the reaction coordinate, which is then integrated to recover the free energy profile. For more details, see Supplementary Note 1.

The limitations and justifications of our fixed-potential MD simulations are probed and discussed in Supplementary Note 2.

Data availability

The data that support the plots within this paper and other findings of this study are available from the corresponding author upon reasonable request.

Acknowledgements

Author contributions: XD conceived the research. The experiments were carried out by AHS with assistance from CW, SW and LW under the supervision of YH and XD; and the calculations

were carried out by ZZ under the supervision of ANA. The manuscript was written by AHS, ZZ, ANA and XD.

Competing interests: The authors declare no competing interests.

References

1   Sheng, W. *et al.* Correlating hydrogen oxidation and evolution activity on platinum at different pH with measured hydrogen binding energy. *Nat. Commun.* **6**, 5848 (2015).

2   Nørskov, J. K. *et al.* Trends in the exchange current for hydrogen evolution. *J. Electrochem. Soc.* **152**, J23-J26 (2005).

3   Ledezma-Yanez, I. *et al.* Interfacial water reorganization as a pH-dependent descriptor of the hydrogen evolution rate on platinum electrodes. *Nat. Energy* **2**, 17031-17037 (2017).

4   Bockris, J. M. & Potter, E. The mechanism of the cathodic hydrogen evolution reaction. *J. Electrochem. Soc.* **99**, 169-186 (1952).

5   Schouten, K., Van Der Niet, M. & Koper, M. Impedance spectroscopy of H and OH adsorption on stepped single-crystal platinum electrodes in alkaline and acidic media. *Phys. Chem. Chem. Phys.* **12**, 15217-15224 (2010).

6   Strmcnik, D. *et al.* Improving the hydrogen oxidation reaction rate by promotion of hydroxyl adsorption. *Nat. Chem.* **5**, 300-306 (2013).

7   Zhong, G. *et al.* Determining the hydronium pKα at platinum surfaces and the effect on pH-dependent hydrogen evolution reaction kinetics. *Proc. Natl. Acad. Sci. U.S.A.* **119**, e2208187119- e2208187126 (2022).

8   Govindarajan, N., Xu, A. & Chan, K. How pH affects electrochemical processes. *Science* **375**, 379-380 (2022).

9   Greeley, J., Jaramillo, T. F., Bonde, J., Chorkendorff, I. & Nørskov, J. K. Computational high-throughput screening of electrocatalytic materials for hydrogen evolution. *Nat. Mater.* **5**, 909-913 (2006).

10   Laursen, A. B. *et al.* Electrochemical hydrogen evolution: Sabatier's principle and the volcano plot. *J. Chem. Educ.* **89**, 1595-1599 (2012).

11   Skúlason, E. *et al.* Modeling the electrochemical hydrogen oxidation and evolution reactions on the basis of density functional theory calculations. *J. Phys. Chem. C.* **114**, 18182-18197 (2010).

12   Zhu, S., Qin, X., Yao, Y. & Shao, M. pH-Dependent Hydrogen and Water Binding Energies on Platinum Surfaces as Directly Probed through Surface-Enhanced Infrared Absorption Spectroscopy. *J. Am. Chem. Soc.* **142**, 8748-8754 (2020).

13   Sheng, W., Gasteiger, H. A. & Shao-Horn, Y. Hydrogen oxidation and evolution reaction kinetics on platinum: acid vs alkaline electrolytes. *J. Electrochem. Soc.* **157**, B1529-B1536 (2010).

14   Subbaraman, R. *et al.* Trends in activity for the water electrolyser reactions on 3d M (Ni, Co, Fe, Mn) hydr (oxy) oxide catalysts. *Nat. Mater.* **11**, 550-557 (2012).

15   Durst, J. *et al.* New insights into the electrochemical hydrogen oxidation and evolution reaction mechanism. *Energy Environ. Sci.* **7**, 2255-2260 (2014).

16   van der Niet, M. J. T. C., Garcia-Araez, N., Hernández, J., Feliu, J. M. & Koper, M. T. M. Water dissociation on well-defined platinum surfaces: The electrochemical perspective. *Catal. Today* **202**, 105-113 (2013).

17   Goyal, A. & Koper, M. T. M. The Interrelated Effect of Cations and Electrolyte pH on the Hydrogen Evolution Reaction on Gold Electrodes in Alkaline Media. *Angew. Chem. Int. Ed.* **60**, 13452-13462 (2021).

18   Shen, L.-f. *et al.* Interfacial Structure of Water as a New Descriptor of the Hydrogen Evolution Reaction. *Angew. Chem. Int. Ed.* **59**, 22397-22402 (2020).

19   Cheng, T., Wang, L., Merinov, B. V. & Goddard, W. A., III. Explanation of Dramatic pH-Dependence of Hydrogen Binding on Noble Metal Electrode: Greatly Weakened Water Adsorption at High pH. *J. Am. Chem. Soc.* **140**, 7787-7790 (2018).

20   Chen, M. *et al.* Hydroxide diffuses slower than hydronium in water because its solvated structure inhibits correlated proton transfer. *Nat. Chem.* **10**, 413-419 (2018).

21   Koper, M. A basic solution. *Nat. Chem.* **5**, 255-256 (2013).

22   Li, P. *et al.* Hydrogen bond network connectivity in the electric double layer dominates the kinetic pH effect in hydrogen electrocatalysis on Pt. *Nat. Catal.* **5**, 900-911 (2022).

23   Lamoureux, P. S., Singh, A. R. & Chan, K. pH Effects on Hydrogen Evolution and Oxidation over Pt(111): Insights from First-Principles. *ACS Catal.* **9**, 6194-6201 (2019).

24   Wang, X., Xu, C., Jaroniec, M., Zheng, Y. & Qiao, S.-Z. Anomalous hydrogen evolution behavior in high-pH environment induced by locally generated hydronium ions. *Nat. Commun.* **10**, 4876 (2019).

25   Jung, O., Jackson, M. N., Bisbey, R. P., Kogan, N. E. & Surendranath, Y. Innocent buffers reveal the intrinsic pH- and coverage-dependent kinetics of the hydrogen evolution reaction on noble metals. *Joule* **6**, 476-493 (2022).

26   Sun, K. *et al.* Interfacial water engineering boosts neutral water reduction. *Nat. Commun.* **13**, 6260 (2022).

27   Ding, M. *et al.* An on-chip electrical transport spectroscopy approach for in situ monitoring electrochemical interfaces. *Nat. Commun.* **6**, 7867 (2015).

28   Ding, M. *et al.* On-chip in situ monitoring of competitive interfacial anionic chemisorption as a descriptor for oxygen reduction kinetics. *ACS Cent. Sci.* **4**, 590-599 (2018).

29   Shah, A. H. *et al.* The role of alkali metal cations and platinum-surface hydroxyl in the alkaline hydrogen evolution reaction. *Nat. Catal.* **5**, 923-933 (2022).

30   Giles, S. A. *et al.* Recent advances in understanding the pH dependence of the hydrogen oxidation and evolution reactions. *J. Catal.* **367**, 328-331 (2018).

31   Duan, Z. & Henkelman, G. Atomic-Scale Mechanisms of Electrochemical Pt Dissolution. *ACS Catal.* **11**, 14439-14447 (2021).

32   Chen, J.-W. *et al.* Pseudo-adsorption and long-range redox coupling during oxygen reduction reaction on single atom electrocatalyst. *Nat. Commun.* **13**, 1734 (2022).

33   Li, C.-Y. *et al.* In situ probing electrified interfacial water structures at atomically flat surfaces. *Nat. Mater.* **18**, 697-701 (2019).

34   Martínez-Hincapié, R., Sebastián-Pascual, P., Climent, V. & Feliu, J. M. Exploring the interfacial neutral pH region of Pt(111) electrodes. *Electrochem. Commun.* **58**, 62-64 (2015).

35   Rizo, R., Sitta, E., Herrero, E., Climent, V. & Feliu, J. M. Towards the understanding of the interfacial pH scale at Pt(111) electrodes. *Electrochim. Acta* **162**, 138-145 (2015).

36   Yoo, H.-W., Cho, S.-Y., Jeon, H.-J. & Jung, H.-T. Well-Defined and High Resolution Pt Nanowire Arrays for a High Performance Hydrogen Sensor by a Surface Scattering Phenomenon. *Anal. Chem.* **87**, 1480-1484 (2015).

37   Jorgensen, W. L., Chandrasekhar, J., Madura, J. D., Impey, R. W. & Klein, M. L. Comparison of simple potential functions for simulating liquid water. *J. Chem. Phys.* **79**, 926-935 (1983).

38   Adamo, C. & Barone, V. Toward reliable density functional methods without adjustable parameters: The PBE0 model. *J. Chem. Phys.* **110**, 6158-6170 (1999).

39   Kresse, G. & Joubert, D. From ultrasoft pseudopotentials to the projector augmented-wave method. *Phys. Rev. B* **59**, 1758 (1999).

40   Kresse, G. & Furthmüller, J. Efficiency of ab-initio total energy calculations for metals and semiconductors using a plane-wave basis set. *Comput. Mater. Sci.* **6**, 15-50 (1996).

41   Kresse, G. & Furthmüller, J. Efficient iterative schemes for ab initio total-energy calculations using a plane-wave basis set. *Phys. Rev. B* **54**, 11169 (1996).

42   Kresse, G. & Hafner, J. Ab initio molecular dynamics for liquid metals. *Phys. Rev. B* **47**, 558 (1993).

43   Kresse, G. & Hafner, J. Ab initio molecular-dynamics simulation of the liquid-metal–amorphous-semiconductor transition in germanium. *Phys. Rev. B* **49**, 14251 (1994).

44   Grimme, S., Antony, J., Ehrlich, S. & Krieg, H. A consistent and accurate ab initio parametrization of density functional dispersion correction (DFT-D) for the 94 elements H-Pu. *J. Chem. Phys.* **132**, 154104 (2010).

45   Mathew, K., Kolluru, V. C., Mula, S., Steinmann, S. N. & Hennig, R. G. Implicit self-consistent electrolyte model in plane-wave density-functional theory. *J. Chem. Phys.* **151**, 234101 (2019).

46   Yu, M. & Trinkle, D. R. Accurate and efficient algorithm for Bader charge integration. *J. Chem. Phys.* **134**, 064111 (2011).

47   Nelson, R. *et al.* LOBSTER: Local orbital projections, atomic charges, and chemical-bonding analysis from projector-augmented-wave-based density-functional theory. *J. Comput. Chem.* **41**, 1931-1940 (2020).

48   Chai, J.-D. & Head-Gordon, M. Long-range corrected hybrid density functionals with damped atom–atom dispersion corrections. *Phys. Chem. Chem. Phys.* **10**, 6615-6620 (2008).

49   Schäfer, A., Huber, C. & Ahlrichs, R. Fully optimized contracted Gaussian basis sets of triple zeta valence quality for atoms Li to Kr. *J. Chem. Phys.* **100**, 5829-5835 (1994).

50   Frisch, M. et al. Gaussian 16, Revision C.01 (Gaussian, Inc., 2016).

51   Lu, T. & Chen, F. Multiwfn: a multifunctional wavefunction analyzer. *J. Comput. Chem.* **33**, 580-592 (2012).

52   Steinmann, S. N., Michel, C., Schwiedernoch, R. & Sautet, P. Impacts of electrode potentials and solvents on the electroreduction of CO_2: a comparison of theoretical approaches. *Phys. Chem. Chem. Phys.* **17**, 13949-13963 (2015).

53   Korpelin, V. *et al.* Addressing dynamics at catalytic heterogeneous interfaces with DFT-MD: Anomalous temperature distributions from commonly used thermostats. *J. Phys. Chem. Lett.* **13**, 2644-2652 (2022).

54   Bonnet, N., Morishita, T., Sugino, O. & Otani, M. First-Principles Molecular Dynamics at a Constant Electrode Potential. *Phys. Rev. Lett.* **109**, 266101 (2012).

55   Humphrey, W., Dalke, A. & Schulten, K. VMD: visual molecular dynamics. *J. Mol. Graph.* **14**, 33-38 (1996).

56   Ryckaert, J.-P., Ciccotti, G. & Berendsen, H. J. C. Numerical integration of the cartesian equations of motion of a system with constraints: molecular dynamics of n-alkanes. *J. Comput. Phys.* **23**, 327-341 (1977).

57   Fleurat-Lessard, P. & Ziegler, T. Tracing the minimum-energy path on the free-energy surface. *J. Chem. Phys.* **123**, 1948367 (2005).

58   Sundararaman, R. & Schwarz, K. Evaluating continuum solvation models for the electrode-electrolyte interface: Challenges and strategies for improvement. *J. Chem. Phys.* **146**, 084111 (2017).

59   Gauthier, J. A. *et al.* Challenges in Modeling Electrochemical Reaction Energetics with Polarizable Continuum Models. *ACS Catal.* **9**, 920-931 (2019).

60   Le, D. An Explicit-Implicit Hybrid Solvent Model for Grand Canonical Simulations of the Electrochemical Environment. doi:https://doi.org/10.26434/chemrxiv-2023-z2n4n (2023).

61   Zhang, Z., Wei, Z., Sautet, P. & Alexandrova, A. N. Hydrogen-Induced Restructuring of a Cu(100) Electrode in Electroreduction Conditions. *J. Am. Chem. Soc.* **144**, 19284-19293 (2022).

62   Hanselman, S., Calle-Vallejo, F. & Koper, M. Computational description of surface hydride phases on Pt (111) electrodes. *J. Chem. Phys.* **158**, 014703 (2023).

63   Cheng, D. *et al.* Restructuring and Activation of Cu(111) under Electrocatalytic Reduction Conditions. *Angew. Chem. Int. Ed.* **62**, e202218575 (2023).

64   Cheng, T., Xiao, H. & Goddard, W. A. Full atomistic reaction mechanism with kinetics for CO reduction on Cu(100) from ab initio molecular dynamics free-energy calculations at 298 K. *Proc. Natl. Acad. Sci. U.S.A.* **114**, 1795-1800 (2017).

65   Zhao, X., Levell, Z. H., Yu, S. & Liu, Y. Atomistic Understanding of Two-dimensional Electrocatalysts from First Principles. *Chem. Rev.* **122**, 10675-10709 (2022).

66   Qian, S.-J. *et al.* Critical Role of Explicit Inclusion of Solvent and Electrode Potential in the Electrochemical Description of Nitrogen Reduction. *ACS Catal.* **12**, 11530-11540 (2022).
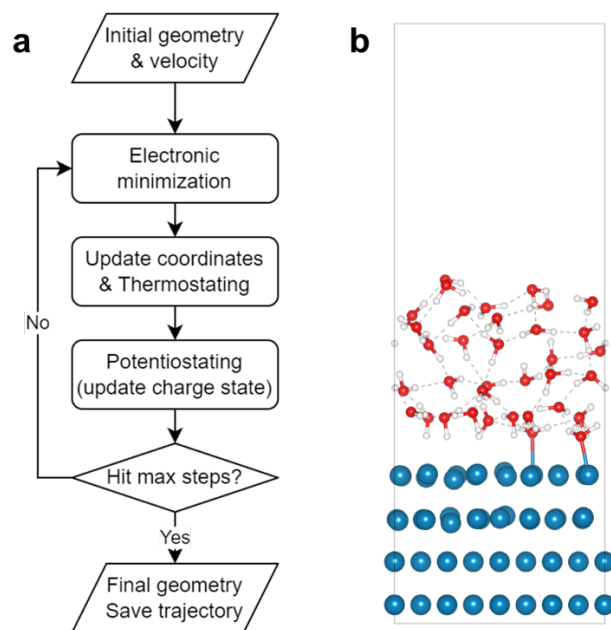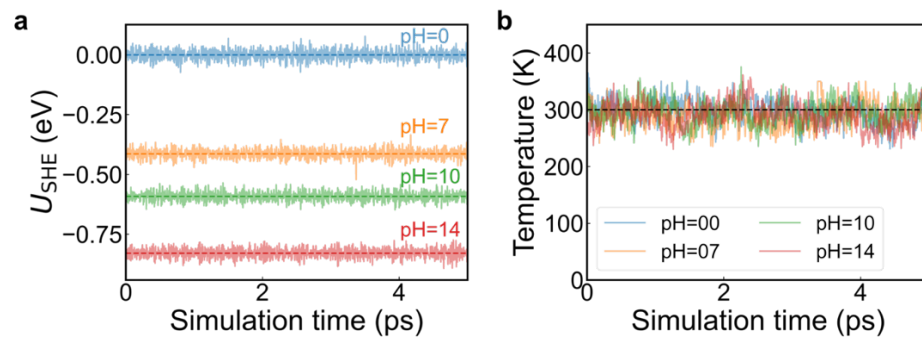
Supplementary Figures
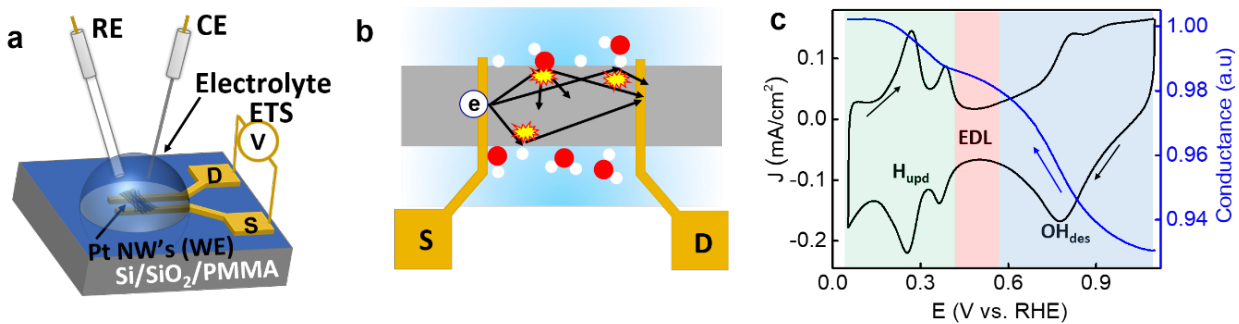
Supplementary Fig. 1| Schematic illustration of experimental setup and working principle of the on-chip electrical transport spectroscopy (ETS) measurement. (a) on-chip PtNWs device for ETS measurements and **(b)** electrons scattering mechanism of various adsorbate molecules on PtNWs. **(c)** Typical ETS spectra and cyclic voltammogram with representation of various regions 0.1 M KOH solution (adapted from ref [29]).
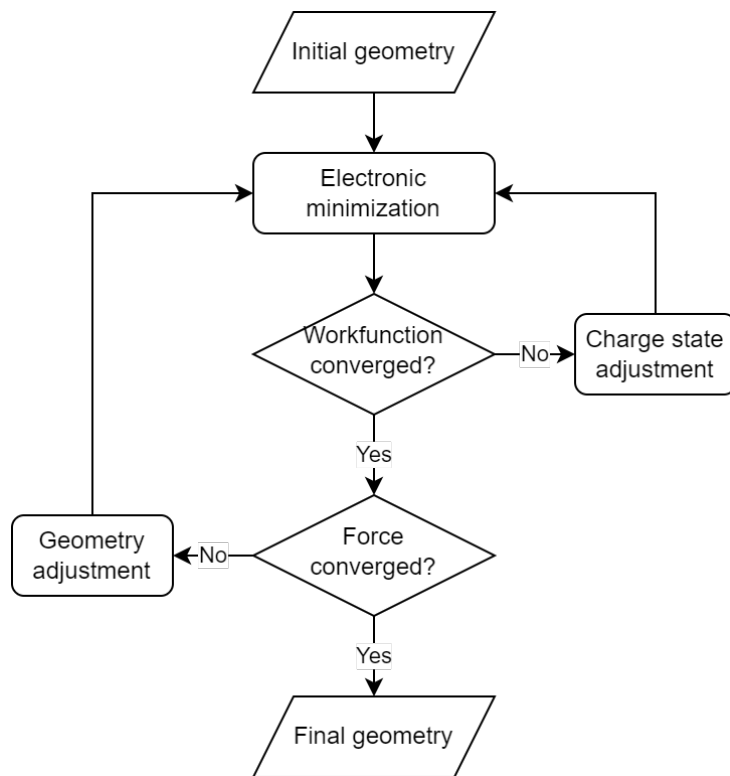
Supplementary Fig. 2| Algorithmic flowchart of the fixed-potential geometry optimization.

Supplementary Fig. 3| (a) Algorithmic flowchart of the fixed-potential (FP) ab initio molecular dynamics (AIMD) simulation and **(b)** A side view of the simulation box used for FP-AIMD.

Supplementary Fig. 4| Validation of the proper potentiostating and thermosetting of the FP-AIMD scheme. The evolution of **(a)** the work function and **(b** the temperature of the systems during 5-ps simulation at different pH levels.
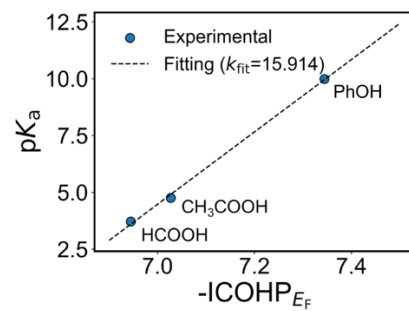
Supplementary Fig. 5| Correlating pK_a with calculated -ICOHP up to Fermi level on an experimental data set of organic acids. The R-square of the fitting is 0.998.
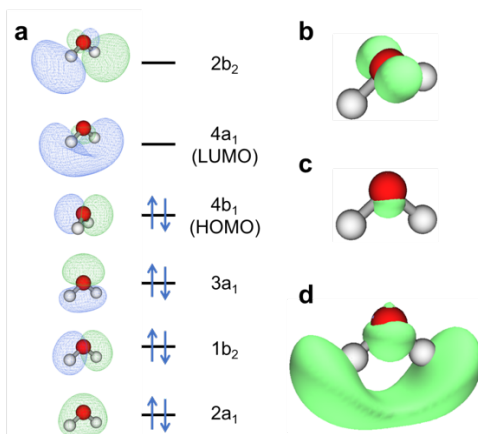
Supplementary Fig. 6| Molecular fragment analysis of charged H₂O. (a) Molecular orbital diagram of
H₂O. The isosurface of **(b)** positive charge on [H₂O]$^+$ at isovalue of 0.02, **(c)** negative charge on [H₂O]$^-$ at
isovalue of 0.02 and **(d)** at 0.005.
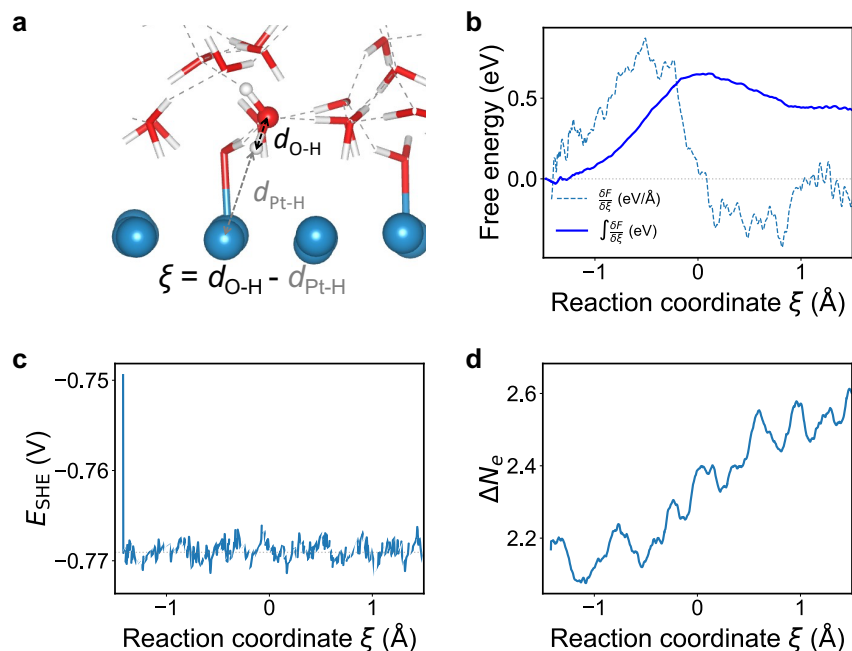
Supplementary Fig. 7| Details of the fixed-potential free energy calculation of water dissociation at pH=14. (a) The definition of reaction coordinate ξ for the water dissociation reaction, with negative values and positive values representing intact and dissociated states of the interfacial water, respectively. **(b)** The free energy gradient and integrated free energy along the reaction coordinate. **(c)** Fluctuation of potential (SHE scale) of the system along the reaction coordinate, with grey dotted line marking the target potential (E_{RHE}=0 V, pH=14). **(d)** Fluctuation in the net number of electrons in the system along the reaction coordination, which indicates the charge transfer between the surface and the electrode (electron reservoir) during the reaction.
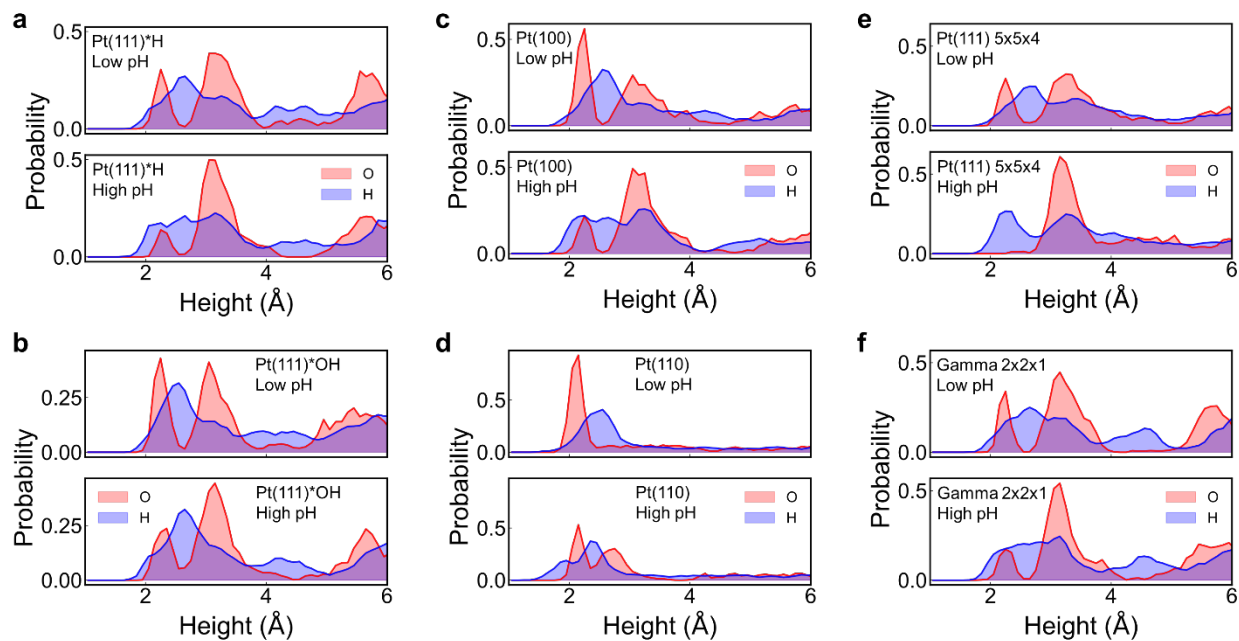
Supplementary Fig. 8| Additional simulations with multiple factors considered. The spatial distribution of O and H in the water layer from fixed-potential MD simulations (each of ca. 10 ps duration) at low and high pH values for **(a)** Pt(111) with *H adsorbate of 1/16 ML coverage, **(b)** Pt(111) with *OH adsorbate of 1/16 ML coverage, **(c)** Pt(100), **(d)** Pt(110), **(e)** a larger $5\times5\times4$ slab of Pt(111), **(f)** with a higher K-points of $2\times2\times1$ Gamma points for reciprocal space sampling.

Supplementary Note 1. Details of the free energy calculation based on fixed-potential MD.

To calculate the free energetic of water dissociation, a rare event, we employed the slow-grow approach to sample uniformly along the reaction coordinate ξ as defined in Supplementary Fig. 7a. To be specific, the reaction coordinate is constrained by the SHAKE algorithm[56] and then varied at a constant rate $\frac{d\xi}{dt}$ of 0.001 Å/fs which is sufficiently slow for all degrees of freedom other than the reaction coordinate to fully equilibrate. The resulted samples constitute a blue moon ensemble where the free energy gradient $\left(\frac{\partial F}{\partial \xi}\right)_{\xi^*}$ at any ξ^* can be calculated based on the mass metric tensor and the Lagrange multiplier associated with the ξ in the SHAKE algorithm.[57] The free energy difference between any two states, ξ_1 and ξ_2, can be calculated by integrating the free energy gradient:

$$\Delta F_{1\to 2} = \int_{\xi_1}^{\xi_2} \left(\frac{\partial F}{\partial \xi}\right)_{\xi^*} \left(\frac{d\xi}{dt}\right) dt$$

By performing integration from the initial state up to any state along the reaction coordinate, we can obtain the free energy profile as exemplified in Supplementary Figure 7b.

Note that the whole configurational sampling is performed under a fixed-potential condition by a theoretical potentiostat which stabilizes the potential of the system around the target potential with minimal fluctuations (Supplementary Fig. 7c). The fluctuation of net number of electrons in the system associated with the reaction can also be tracked along the reaction coordinate, and the charge transfer accompanying the water dissociation is evaluated to be ca. 0.5 |e| (Supplementary Fig. 7d).

Supplementary Note 2. Limitations and justifications of our fixed-potential MD simulations.

In this work, we study the pH effect at the same electrode potential (RHE scale) by aligning the workfunction of the system to different absolute potentials (SHE scale) according to the Nernst equation. Such practice corresponds to adjusting the surface charge in response to pH changes, and we assume the charge transfer between the electrode and the catalyst surface to be much faster than the solvation dynamics at the interface, so that the charge state and the workfunction can fully equilibrate after every local optimization or MD step.

We do not include any explicitly solvated hydroxides in this work to model pH effect because: (i) Given the affordable system size, it is not possible to continuously tune the hydroxide concentration in the pH range of interest (7 to 14). (ii) Within the grand canonical DFT + hybrid solvation scheme, presence of explicit charged solutes can cause artifacts where the counter charge density leaks into the solvation shell and compete with the actual solvent molecules in solvating the charged solute.[58-60] Such artifacts would cause unphysical dynamics of the solvents and the interfacial charge distribution; hence we do not include any explicit solvated hydroxide or cations in the simulation box. (iii) The concentration of solvated hydroxide in the contact layer of the cathode is expected to be negligible. Even if present, they would not disrupt the solvation structure like the larger cations[29] and hence should not alter the overall statistics of interfacial water orientation qualitatively.

The effect of surface adsorbates are probed by additional simulations with surface coverage of *H or *OH, at low or high pH (Supplementary Fig. 8 a-b). The pH response of interfacial water orientation remains qualitatively the same as the case of bare Pt surface (Fig. 4c). We do not consider a very high coverage case, since the metal surface can undergo more complex H-induced restructurings,[61-63] which would require more sophisticated configuration sampling and is beyond the scope of this study. In addition, herein we are particularly interested in the organization of water over the bare Pt sites where water dissociation can take place, instead of the adsorbate occupied sites.

Since the sample is a polycrystalline Pt nanowire, we have also performed additional simulations at low or high pH on Pt(110) and Pt(100) surfaces which have different surface Pt coordination states and different adsorption energetics from those pt Pt(111). The results of these simulations, as shown in Supplementary Fig. 8 c-d, indicate that while the shape of the spatial distribution of

O and H may be slightly different from those of Pt(111), the reorientation of interfacial water from O-down to H-down when pH goes from low to high is qualitatively consistent with the case of Pt(111). This suggests that the pH-dependent surface charge, rather than the surface structure, is the dominant factor driving the observed water reorientation.

We have also performed simulations with a larger slab size of $5 \times 5 \times 4$ Pt(111), which is approximately 156% of the surface area of the original slab, and with a higher k-point of $2 \times 2 \times 1$ Gamma point to sample the reciprocal space, at low or high pH values. Both sets of simulations (Supplementary Fig. 8e-f) yield pH-response of the interfacial water orientation consistent with Fig 3c and the main conclusions of this study. While larger unit cells would be preferable, computational limitations and simulation time to equilibration make this challenging for ab initio molecular dynamics simulations. Our previous works and those of others using similar methods[29,64-66] have shown that our cell size is sufficient to avoid spatial correlation issues from periodic boundary conditions and yield correct spatial of interfacial water. Moreover, the orientational switch of interfacial waters has an electronic origin (pH-dependent surface charge) that is not strongly dependent on the surface area or the thickness of the water slab.

While we acknowledge that many realistic factors (independent or interdependent) may influence the solvation structure of the interfacial waters, our additional tests in Supplementary Fig 8 demonstrate that the pH trend remains qualitatively consistent regardless of these additional complexities probed herein. It is possible that the presence of other complexity may "shift" the distribution of water orientation and account for the ~1 pH unit discrepancy compared to the experimental "critical pH" of the orientational switch, but the probed complexities should not be the major factor in driving this pH-dependent and phase transition-like reorganization of interfacial water.